Numerical Simulations of Ionic Wind Induced by Positive DC-Corona Discharges

Francesco Picella, David Fabre, Franck Plouraboué

Numerical simulations of ionic wind induced by positive DC-corona discharges

Francesco Picella, David Fabre, and Franck Plouraboué
Institut de Mécanique des Fluides de Toulouse (IMFT) Université de Toulouse, CNRS, INPT, UPS, Allée du Pr. Camille Soula, 31400 Toulouse, France.
(Dated: April 17, 2024)

This paper analyzes ionic wind production as well as propulsive force in various electrode configurations in atmospheric conditions. From considering the aerodynamical forces in addition to previously considered Electric ones, new predictions for steady-state forces and ionic wind flow velocity are successfully compared with experimental measurements, providing a very convincing quantitative evidence of the predictive capabilities of drift-diffusion modeling associated with one-way Coulomb forcing of Navier-Stokes equations for ionic wind generation. Furthermore, various electrode configurations are analyzed, some of them streamlined, reducing downstream collector(s) wake(s) on the one hand, besides providing additional thrust on the other hand. The quantification of these additional thrust are analyzed, physically discussed and explored in various configurations.

NOMENCLATURE

(Nomenclature entries should have the units identified)

$AR = r_c/l_c$	=	Aspect ratio of streamlined collector profiles.
d	=	face-to-face emitter collector distance
D_ρ	=	$[m^2/s]$ Diffusivity of unipolar charges in air
ϵ_0	=	dielectric permittivity of free space
E	=	$[V \cdot m^{-1}]$ Electric field
E_a	=	$[V \cdot m^{-1}]$ Imposed electric field at the emitter edge from Kaptzov hypothesis
Γ	=	Corona discharge edge where Kaptsov constant electric field is applied
l_c	=	cord length of streamlined collectors
L	=	span-wise length of collectors
μ	=	$[m^2/V \cdot s]$ unipolar charges electric mobility
μ_f	=	$[kg \cdot m^{-1} \cdot s^{-1}]$ fluid viscosity
p	=	$[Pa]$ fluid pressure
$Pe = \mu V/D_\rho$	=	electro-drift Péclet number
ϕ	=	$[V]$ Electric potential
Θ	=	boundary-layer momentum thickness
ρ	=	$[C/m^3]$ charge density
ρ_f	=	$[kg/m^3]$fluid density
r_e	=	$[m]$ emitter radius
r_c	=	$[m]$collector radius
σ	=	$[Pa]$ stress tensor
s	=	$[m]$ collector inter-space
$\mathbf{T} = \mathbf{T^E} + \mathbf{T^A}$	=	$[N]$ total Thrust
$\mathbf{T^E}$	=	$[N]$ EAD contribution to Thrust
$\mathbf{T^A}$	=	$[N]$ aerodynamic contribution to Thrust=drag
$\mathbf{u}$	=	$[m \cdot s^{-1}]$ fluid velocity field
V	=	$[V]$ Applied high-voltage at emitter
x, y	=	$[m]$ Cartesian coordinates
Ω	=	Fluid domain
$\partial\Omega$	=	Edge of Fluid domain
$\partial\Omega_e$	=	Edge of emitter identified with the edge of the corona discharge
$\partial\Omega_c$	=	Edge of collector

I. INTRODUCTION

The renewed interest for Ionic wind propulsion is associated with almost silent, electric propulsion without moving parts [1, 2]. Even if electric propulsion is now well-established in spatial applications, it is much less advanced in atmospheric conditions where the physical mechanisms of charge creation and acceleration are very distinct from the one found in the spatial context. This research area is nevertheless expanding partly motivated by the growing trend towards reduction of fossil fuel. In this expanding field of research recent developments have been dedicated to experimentally analyze the propulsive and electrical performances of various electrode configurations, e.g [2–7] to cite only a few. In this context, a plasma is generated in narrow regions of space where ionization occurs, and subsequently drifts away from the action of an electric field. In the "drift region" (namely, away from the regions of ionization), the drifting charges accelerate neutral air through collisions, resulting in ionic wind production.

In this contribution we examine more specifically the case of the corona discharge source which is associated with a high DC-potential electrode of small size subsequently called an "emitter". The corona discharge modeling is complex (e.g [8]) so that many studies in the field rely on the Kaptzov hypothesis. The latter allows to avoid the detailed description of corona discharge by imposing a constant electric field at the surface of the emitter noted $\partial\Omega_e$ as done in [9**?** , 10]. The precise value of this imposed electric field is either empirical [11] or provided by some recent asymptotic analysis [12]. In the later, the Kaptzov hypothesis has been derived theoretically in the case of an axi-symmetric geometry, where a constant normal electric field emerging from the thin corona discharge region has been found proportional to the Townsend ionization electric field.

Numerous researches are currently on the way to optimize the propulsion properties, either by exploring the potentia,l of multi-electrode configurations [6, 13–16], or by modifying the geometry of the electrodes.

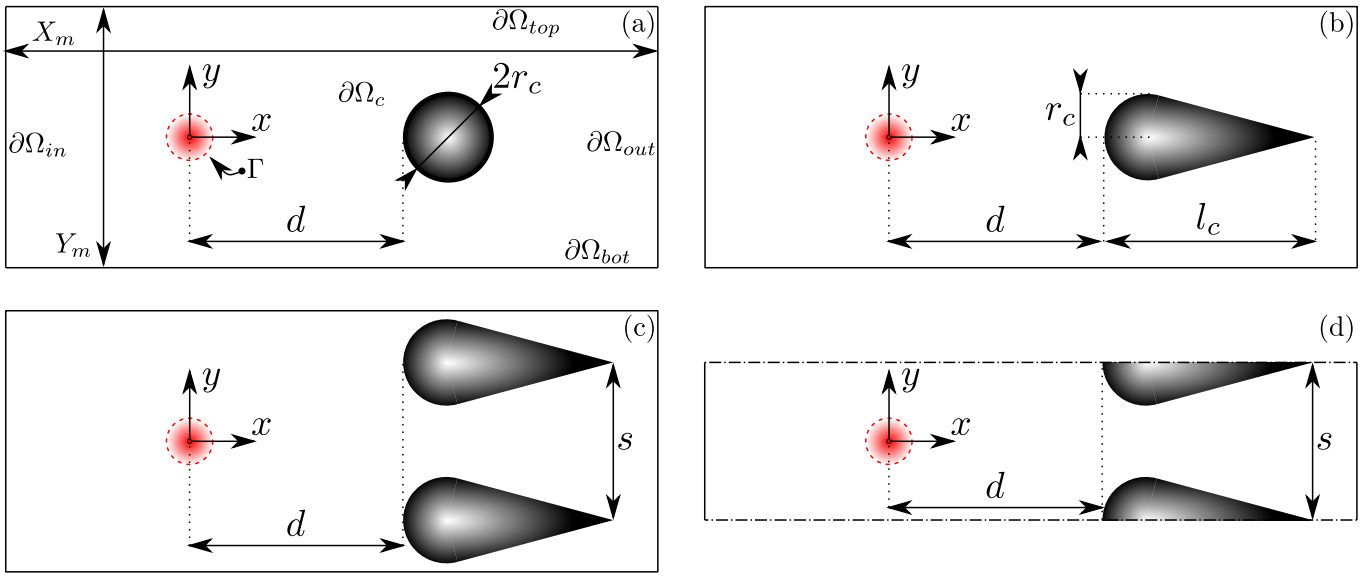

FIG. 1: Sketch of the various configurations analyzed in this study. (a) 1 Emitter/1 cylindrical Collector (1E/1C) configuration (b) 1 Emitter/1 streamlined drop-shaped Collector (1E/1S) (c) 1 Emitter/2 streamlined drop-shaped (1E/2S) (d) Periodic array of Emitters and streamlined drop-shaped collectors (NE/NS).

In particular, elongated collector shapes (referred as "streamlined" in the sequel) have been previously proposed and investigated [3, 4]. More precisely, streamlined collectors are obviously more aerodynamically favorable [4, 15] among which drop-shaped ones have shown interesting propulsive performances [3, 4, 15]. This is why we wish to investigate how such configurations are changing the propulsive capabilities. In special particular cases some analytical results concerning the EHD thrust T^A have been established. In one dimensional configurations it has been found in [17–19] that T^A is linearly related to the total current I

$$\mathrm{T}^A = \frac{Id}{\mu}, \tag{1}$$

where μ the unipolar charges mobility, and d the emitter/collector distance. In quasi-one dimensional configurations T^A has been found to reach a Mott-Gurney law [20], and (1) has been extended to more general configurations such as asymptotically far emitter-collector ones [19, 21]. Nevertheless the aero-dynamic contribution to the force has not been clearly investigated yet, and is very much configuration dependant, as noted in [23]. Numerical modeling of ionic wind propulsion has rarely considered the aerodynamics contributions to thrust whilst focusing on the contribution of electrostatic forces (e.g [22]) obtained by solving the drift-diffusion equations for electric potential and the charge density exept for the case of quasi-stationary Dielectric Barrier Discharge (DBD) around an airfoil studied in [23]. Steamming from [22], we analyze atmospheric ionic wind thrusters both considering aerodynamics and electrostatics, solving for Coulomb forcing of the Navier-Stokes equations. This provides an improved prediction of the thrust force containing both an electrostatic contribution and an aerodynamical force (the drag). The paper is organized as follows. Section II discuss the methods used to obtain converged 2D steady-state Navier-Stokes solutions generating ionic-wind jets, and provides numerical convergence studies. Section III A examines and illustrates the comparison between the predicted EAD forces and experimental measurements, as well as averaged 2D-PIV data from [21] with their numerical modeling. Section III B examines and analyses the propulsive performance gain of new streamlined collectors configurations, for which the associated main physical ingredients are discussed.

II. METHODS

A. Configurations under study

This paper considers four distinct configurations, as depicted in figure 1: (a) a simple 'test case' configuration for which a single emitter/collector pair (denoted 1E/1C) having a cylindrical shape are used as reference for comparison and validation; (b) a similar configuration with a single streamlined collector (denoted 1E/1S); (c) a single emitter

coupled with two collectors having either cylindrical shape (denoted 1E/2C) or streamlined shape (denoted 1E/2S); and (d) A periodic assembly of emitter/collector (noted NE/NS). As in [4, 15, 24], the geometry for the streamlined collectors is a "drop-shape" profile corresponding to a leading edge with circular shape connected to a triangular tail. We note $AR = r_c/l_c$ the aspect ratio of such profiles. In the following, the upstream face of each collector is chosen with the same radius of curvature so as to analyse specifically the effect of distinct downstream shape. A high electric potential V is imposed at emitter(s) whereas a ground potential 0 is considered at collector(s). Even if these boundary conditions are imposed in every configurations, instead of discussing the obtained results versus the imposed potential drop V, it has been found usefull to rather consider the corresponding imposed external electric field V/d, which is sometimes denotes $E^{ext} \equiv V/d$. Thus in the sequel, "imposed external electric field" refers to a given couple of constant potential drop to distance d ratio, i.e $E^{ext} = V/d$. Obviously in neither case the electric field is constant anywhere but the boundary conditions are just stated such that the imposed external electric field E^{ext} is given.

B. Formulation and numerical method

The modeling adopted here is a one-way coupling approach, which consists in (i) solving the electrostatic problem governing the charge densities and electric potential, and (ii) subsequently solving the Navier-Stokes equations including a forcing term coming from the electric problem. The one-way coupling approximation is based upon the hypothesis that convective effects are small compared to electro-convective ones. Hence, the electro-convective dimensionless ratio $M_{ce} = U/\mu E^{ext}$ (M symbol has been chosen since, like the Mach number, this number is a velocity ratio comparing the fluid velocity with another velocity) based upon the convective velocity U to the ion drift velocity μE^{ext} is a small parameter . In the sequel, since the mobility ratio of charges in air is $\mu = 2.10^{-4} SI$ with an imposed potential $V = 20\,kV$, and distance $d = 4\,cm$ one finds $\mu E^{ext} = 100\,m.s^{-1}$ so that for considered external velocity fields U of the order of few meter per second, $M_{ce} \ll 1$, i.e is of the order of $M_{ce} \approx 10^{-2}$. This approximation is considered in the previous literature in the context of moderate advective velocity. In the case where advective effects are larger, two-way coupling effects should be considered which are discarded here. Two-way couplings involve a feed-back of the fluid velocity whithin the ion drift flux conservation, and possibly, if compressibility effects arise, within the ion mobility parameter which depends on the fluid density. They are difficult to take into account because they involve higly hyperbolic non-linear couplings. In the context of this study, there are nevertheless not clearly relevant.

1. Electrostatic problem

The electrostatic problem is solved using the method detailled in [22]. The Poisson problem for the electric potential ϕ $[V]$ reads

$$\Delta\phi = -\frac{\rho}{\epsilon_0}, \tag{2}$$

with ϵ_0 the dielectric permittivity of free space and ρ $[C/m^3]$ the (positive) charge density. The conservation of charges leads to a drift/diffusion equation as follows,

$$\nabla \cdot (-\mu\rho\nabla\phi - D_\rho \nabla\rho) = 0, \tag{3}$$

with charge mobility μ $[m^2/V \cdot s]$, and charge diffusivity D_ρ $[m^2/s]$. A constant electric potential is applied between the electrodes, nearby the emitter surface $\partial\Omega_e$ and collector one $\partial\Omega_c$

$$\phi|_{\partial\Omega_e} = V \tag{4}$$

$$\phi|_{\partial\Omega_c} = 0. \tag{5}$$

whereas a Kaptzov approximation is used by prescribing a constant electric field nearby the emitter(s)

$$\nabla\phi \cdot \mathbf{n}|_{\partial\Omega_e} = E_a \tag{6}$$

with E_a (detailed in [22]) either provided by Peek's formula [11] or the one developed in [12].

The charge mobility is taken as $\mu = 2 \cdot 10^{-}4[m^2/V \cdot s]$ [18, 19], and the charge diffusivity D_ρ is such that the Péclet number $Pe = \mu V/D_\rho$ (correcting Pe definition in [22]) associated with the charge transport is very large, typically $Pe > 10^4$, so that the problem is strongly hyperbolic. Once the electric problem is solved, the corresponding electric thrust exerted along the electrodes can be obtained by integrating the local coulomb force over the domain

$$\mathbf{T}^E = \int_\Omega (-\rho\nabla\phi) dV \tag{7}$$

2. Fluid problem

Regarding the fluid flow problem, the gas is considered as an incompressible fluid with density ρ_f and viscosity μ_f. Looking for a steady flow solution, the velocity field $\mathbf{u}$ and pressure field p are governed by the steady Navier-Stokes equations as follows :

$$\rho_f \mathbf{u}\cdot\nabla\mathbf{u} = -\nabla p + \mu_f \Delta\mathbf{u} + \rho\mathbf{E}, \qquad \nabla\cdot\mathbf{u} = 0. \tag{8}$$

where $\mathbf{E} = -\nabla\phi$ stands for the local electric field. These equations are complemented by no-slip velocity at emitters & collector surfaces $\partial\Omega_e$ & $\partial\Omega_c$,

$$\mathbf{u}|_{\partial\Omega_e} = \mathbf{0} \quad \& \quad \mathbf{u}|_{\partial\Omega_c} = \mathbf{0}. \tag{9}$$

The boundary conditions at the external boundaries of the computational domain are treated as follows. First, a stress-free "outlet" condition is chosen over the downstream and lateral boundaries

$$\sigma\cdot\mathbf{n}|_{\partial\Omega_{top}} = 0 \quad \& \quad \sigma\cdot\mathbf{n}|_{\partial\Omega_{bot}} = 0 \quad \& \quad \sigma\cdot\mathbf{n}|_{\partial\Omega_{out}} = 0, \tag{10}$$

with stress-tensor $\sigma = -p\mathbf{I} + \mu_f(\nabla\mathbf{u} + \nabla\mathbf{u}^T)$. Secondly, at the inlet boundary $\partial\Omega_{in}$, an imposed inlet velocity and tangential stress-free conditions are imposed

$$\mathbf{u}\cdot\mathbf{n}|_{\partial\Omega_{in}} = U_{in} \quad \& \quad \mathbf{t}\cdot\sigma\cdot\mathbf{n}|_{\partial\Omega_{in}} = 0, \tag{11}$$

Note that although the fluid is theoretically at rest away from the electrodes, a small value of U_{in} has to be specified in (9) to avoid numerical divergence associated with flow entrainment. This point is discussed in more details in appendix IV. Once the fluid problem is solved, the corresponding force exerted along the electrodes is obtained as follows

$$\mathbf{T}^H = \int_{\partial\Omega_e\cup\partial\Omega_c} \sigma\cdot\mathbf{n} dS. \tag{12}$$

This aerodynamical force is obviously a drag force acting in the direction opposite to the electric thrust $\mathbf{T}^E$, so that the total force $\mathbf{T} = \mathbf{T}^E + \mathbf{T}^A$ exerted along the electrodes is smaller than $\mathbf{T}^E$.

This one-way coupling formulation is valid as far as the typical convective velocity U is small compared to the electro-drift one $\mu E = \mu V/d$. To be specific, since the effective charge mobility of positive charges has been evaluated to be $\mu \simeq 2.10^{-4}[m^2V^{-1}s^{-1}]$ [18, 19], for an applied external electric field $E = V/d = 5.10^5$ $[V/m]$ the electro-drift velocity is is typically $\mu E \simeq 100[m/s]$ in ambient air. Hence, a one-way approach should provide a reasonable approximation as long as the ambient far-field velocity U_{in} is smaller than 10 $[m/s]$.

3. Numerical methods

Both sets of equations governing the electric problem and the fluid problem are solved using the finite-element software Freefem++ [25], and all computations (mesh generation and adaptation, problem's computations, post-processing) are monitored thanks to StabFem interface [26]. The electric problem is solved as in [22]. In brief, dimensionless equations are considered using r_c as the reference length scale, V as a reference potential, $\epsilon_0 V/r_c^2$ as a reference charge. The equations are then turned into a weak formulation subsequently solved using a Newton iteration method. Note that a regularization technique introduced in [22], is used to enforce a homogeneous distribution of the charges in the vicinity of the emitter and to avoid unphysical phenomena related to the hyperbolic nature of the equations. Likewise, the fluid problem is non-dimensionalyzed using the reference ionic wind velocity $U = (V/r_c)\sqrt{\epsilon_0/\rho_f}$ obtained from balancing the Navier inertia term with the electric Coulomb forcing term. This reference ionic wind velocity U is associated with the Electro-forced Reynolds number $Re_e = (V/\nu_f)\sqrt{\epsilon_0\rho_f}$ which is used to set dimensionless Navier-Stokes equations as in [24]. Hence, along with the classical Reynolds number $Re_a = (U_{in}/\nu_f)/\rho_f$ there are two dimensionless number in the problem. The ratio $(Re_e/Re_a)^2$ is sometimes called the Masuda number [**?**].

The equations are then solved using Newton iteration following the procedure detailed in [26].

It is interesting to mention that, in these computations, mesh adaptation is extensively used following procedures detailed in [26]. In short, after computing the electric quantities (ϕ, ρ) and fluid quantities $(\mathbf{u}, p)$ using an initial mesh, a new mesh is generated with a refinement controlled by the gradients of these fields, so that the solution is projected back on the obtained new mesh, and recomputed. Continuation is also used, meaning that while performing

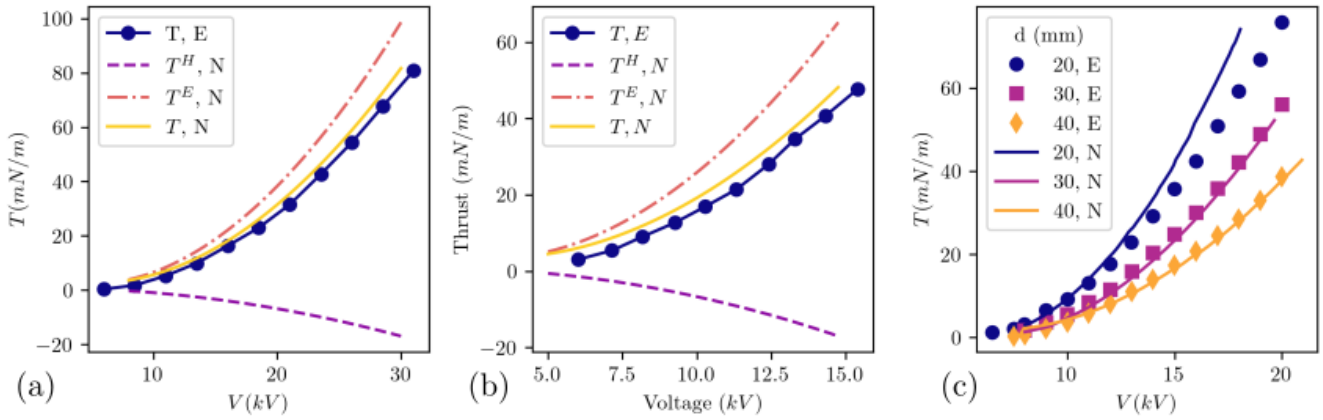

FIG. 2: Comparison between various experimental thrust measurements and numerical predictions in the 1E/1C configuration (E) stands for experiments (N) for numerical predictions. (a) Data from [28] ($r_e = 50\mu m, r_c = 1cm$, d=40mm) comparing the relative contribution of the electric thrust T^E and total drag force $-T^H$ in the total thrust T . (b) Data from [18] ($r_e = 12.5\mu m, r_c = 6cm$; $d = 20$mm) same conventions as a. (c) Data from [27] ($r_e = 50\mu m, r_c = 1.5cm$) for various face-to-face emitter/collector distance d.

loops over parameters, the solution obtained from previous sets of parameters is used as an initial condition for the Newton iterations. It is worth pointing out that the combination of Newton iteration, continuation method, and mesh adaptation makes the method particularly efficient. For instance, solving the electric and fluid problems starting from a previous solution represents only a few minutes of computation on a standard laptop.

III. RESULTS

A. Comparison with experiments for 1E/1C and 1E/2C configurations

In order to test the predictive capability of our modeling and numerical framework, let us first consider the simplest 1E/1C configurations for which many experimental results are available from the literature.

Figure 2a displays the total force T along with its electrical T^E and aerodynamic (drag $-T^A$) components for a configuration studied experimentally by [12].

As previously observed in [22], the thrust T^E computed from the single electrical problem overestimates the experimentally observed force by about 20%. [22] conjectured that the discrepancy was due to the aerodynamic drag, missing in their analysis. Our present results confirm this conjecture and shows that the total force T computed from our modeling is in remarkable agreement with the experiments, with an error of order 1% in this case. Figure 2b & 2c considers other 1E/1C configurations corresponding to experimental data sets from [18] and [27] for various face-to-face distance d between emitters and collectors. Figure 2c shows an accurate prediction obtained within 1% for the two largest distances $d = 30, 40$mm compared to [27] measurements whilst a slight 10% over-prediction in the case of the smaller distance $d = 20$mm is found both in figure 2b & 2c for two distinct measurements [18, 27]. The latter might be attributable to the streamer regime arising for increasing applied external electric field V/d. However, it is interesting to mention that even in this case, the addition of aerodynamic effect to EAD one provide a very convincing accuracy of the proposed modeling.

Even though customary in fluid mechanics, such a quantitative matching between experiments and numerical modeling with about 1% accuracy is seldomly encountered in low-temperature plasma physics, hence worth mentioning here. Furthermore, it is also interesting to add that no parameter fitting has been used for these predictions since all geometrical and electrical parameters have been taken from experiments. Only two additional classical ingredients of drift-diffusion models have been chosen : the Peek law [11] for the normal electric field imposed at the emitter, and the positive ion mobility $\mu_p = 2 \cdot 10^-4 m^2/s$, a value already used in [22] and various other studies.

Figure 3 then compares the numerical predictions for the ionic wind flow-field with time-averaged PIV results from [12] in a similar 1E/1C configurations, for various applied voltages. The upstream flow-field structures in the left & right panels of Figure 3 are strongly analogous, not only concerning the observed streamlines, but also for the reported velocity amplitude. On the other hand, differences are observed in the "wake" region located just downstream of the

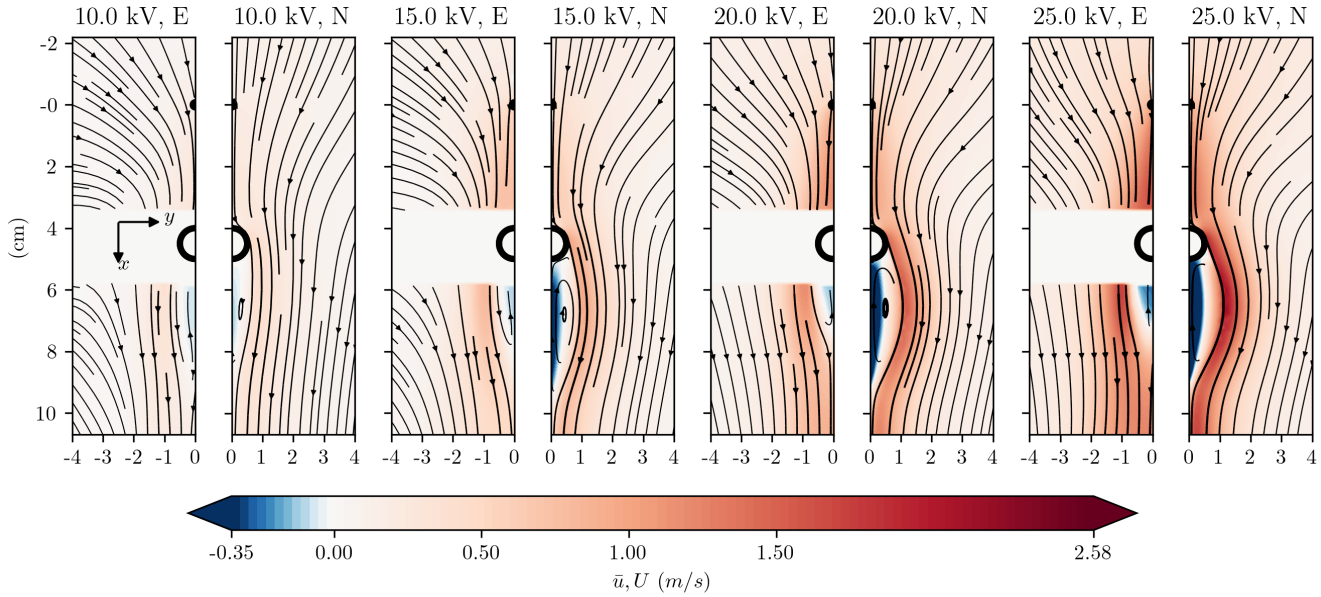

FIG. 3: Comparison between PIV measurements and ionic wind predictions for 1E/1C configurations. Each successive twin-panels represent twin Experimental/Numerical single-sided symmetric configuration. Four 1E/1C configurations ($r_e = 50\mu m, r_c = 1cm$) having equal face-to-face emitter/collector distance $d = 4$cm but distinct voltage difference of 10, 15, 20 & 25 kV are depicted. For each of the four twin-panels, the left one is a 2D-PIV mean-flow field $\overline{u}_x$ experiment and its streamlines obtained in [12] compared with a numerical steady solution u_x on the right.

collector. This region is occupied by a recirculation bubble corresponding to negative values of the streamwise velocity u_x. Inspection of the figure shows that the recirculation bubbles observed in experiments are always less extended and less intense than those predicted by our numerical results. This difference is most likely explained by the fact that in the experiments, the wake is unsteady and characterized by a large amplitude oscillation related to Von Karman-like vortex shedding. Accordingly, the experimental results displayed in figure 3 correspond to the time-averaged "mean flow", which differ from the steady solution of the Navier-Stokes equation obtained for the same parameters (called "base flow" in the aerodynamic stability community) computed using our method. The fact that the recirculation bubbles are always more intense in base–flow calculations that observed from mean–flows is well known (Cf e.g. [26]). It is however remarkable that despite the fact that steady–flow assumption is not relevant in the entire voltage range, thrust numerical predictions are in excellent agreement with experimental results.

A more quantitative comparison of velocity fields is provided in figure 4 which compares the axial velocity profiles at three different x-locations. Upstream from the collector (plot 4a), the axial velocity profile corresponds to a jet, and is well predicted by the computations (the maximum velocity and the jet width being close within 10%). It is interesting to note that, for the 20kV case of figure 4a, the observed 10% difference between numerical predictions and experimental velocity profile's peak is consistent with the mismatch oberved in figure 2c's total thrust for 20kV. At an axial position located beyond the wake region (plot 4c), the axial flow returns to a jet, and is again correctly predicted by numerical results (up to a 15% matching for low voltages, and a little more for highest ones). On the other hand, in the wake region, (plot 4b), the differences are larger. Hence, eventhough for some electric potential difference the thrust missmatch between numerical predictions and experimental measurements reported in figure 2 can be very low, it is however not so clear for the velocity field predictions. This possible inconsistency has to be tempered by the fact that since the total thrust T decomposes into an intrinsic electric part T^E and an aerodynamic one T^A, e.g. $T = T^E + T^A$, both do not equally contribute. As reported in [22] in most cases, T^E is larger than T^A (in some configurations such as 1E/2C as large as 90%) so that a poor prediction in the velocity field does not have a strong impact on the total thrust evaluation.

Let us now turn to 1E/2C configurations, as illustrated in figure 5. Compared to the previous cases, the relevance of the wake structures weakens since the ionic wind is largest in the central region in front of the emitter, so that, for two collectors sufficiently apart (2cm) the downstream wake is progressively reduced (figure 5 middle) and even not visible

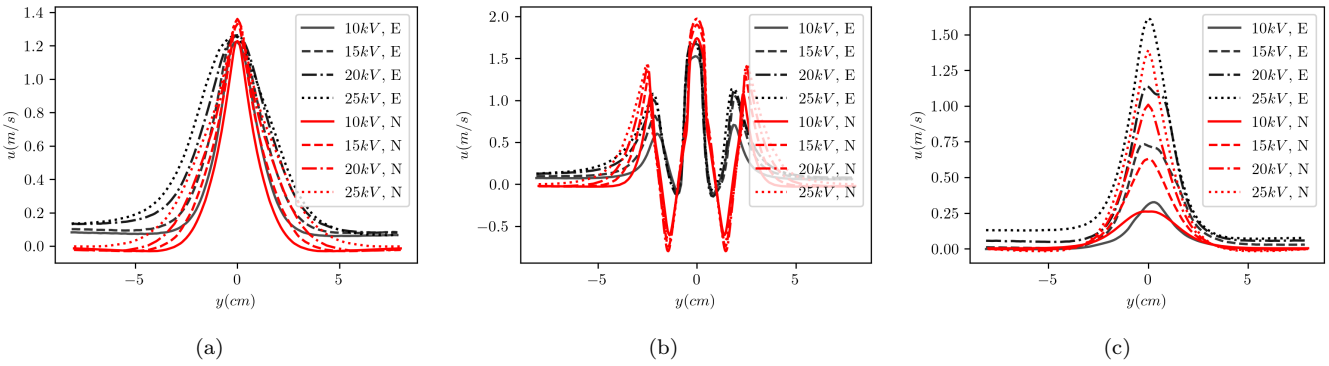

(a) (b) (c)

FIG. 4: Comparison between predicted velocity profiles and PIV experiments from [12] in the 1E/1C configuration ($r_e = 50\mu m, r_c = 1cm$) face-to-face emitter/collector distance $d = 40mm$, for various applied voltages. (E) stands for experiments (N) for numerical predictions . (a) at 2cm uptream from collector (b) 2cm downstream from collector (c) 4 cm downstream from collector.

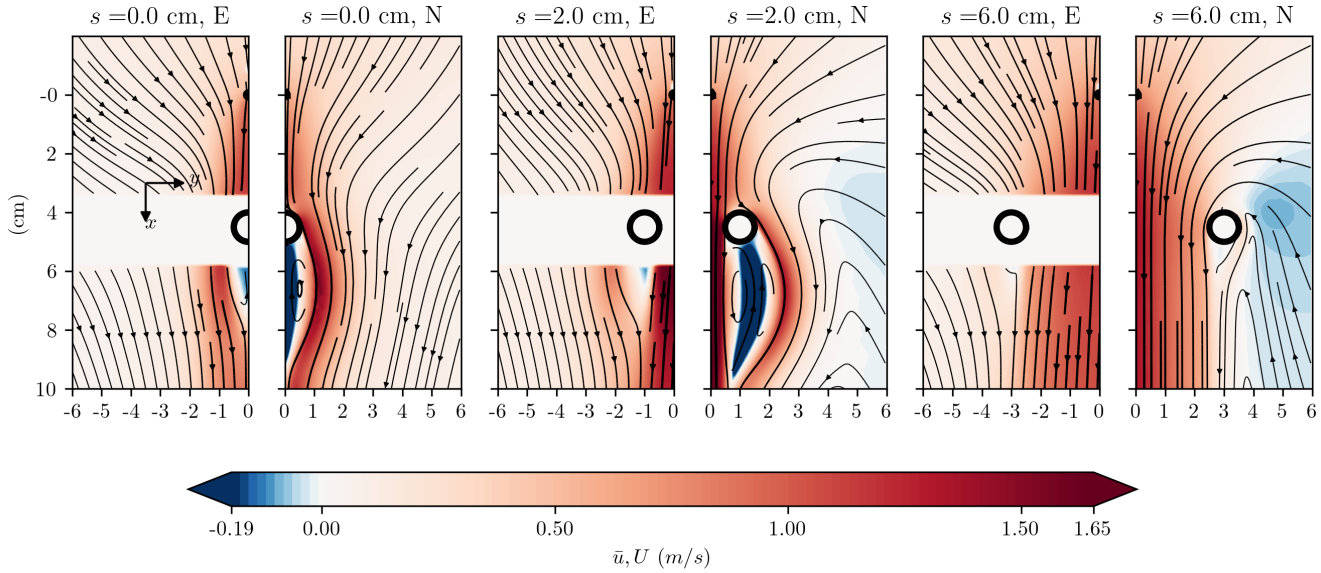

FIG. 5: Same conventions as Fig. 3 for comparing wake shading and flow fields between 1E/1C and 1E/2C configurations from [12] experimental data ($r_e = 50\mu m, r_c = 1cm$). Each successive twin-panels represent twin Experimental/Numerical single-sided symmetric configuration. Left : 1E/1C configuration ($s = 0$). Midle : 1E/2C configuration $s = 2$cm Right 1E/2C configuration $s = 6$cm.

anymore for $s = 6$cm (figure 5 right) where the wake is too small to be seen inside the partially covering experimental domain (the white strip surrounding the experimental collector velocity field is due to the optical obstruction from the electrically insulating frame of [12]'s experimental setup). In this configuration the comparison between experiments and numerical simulations is quantitatively very convincing, as provided by the velocity amplitude prediction as well as the width of the ionic-wind jet downstream the emitter. Note that this configuration has been found to produce the highest thrust in [19, 28], a feature easy to understand from the focussed ionic wind central jet visible downstream the collectors in the right panel of figure 5. In this 1E/2C configuration, Figure 6 shows that the external electric field is the main control parameter for the ionic wind intensity production, since varying the distance d whilst keeping a constant imposed external electric field $E = V/d$ in the various panels does change not much the ionic wind velocity produced between the emitter and the collector either in experiments or numerical simulations. Here again, the

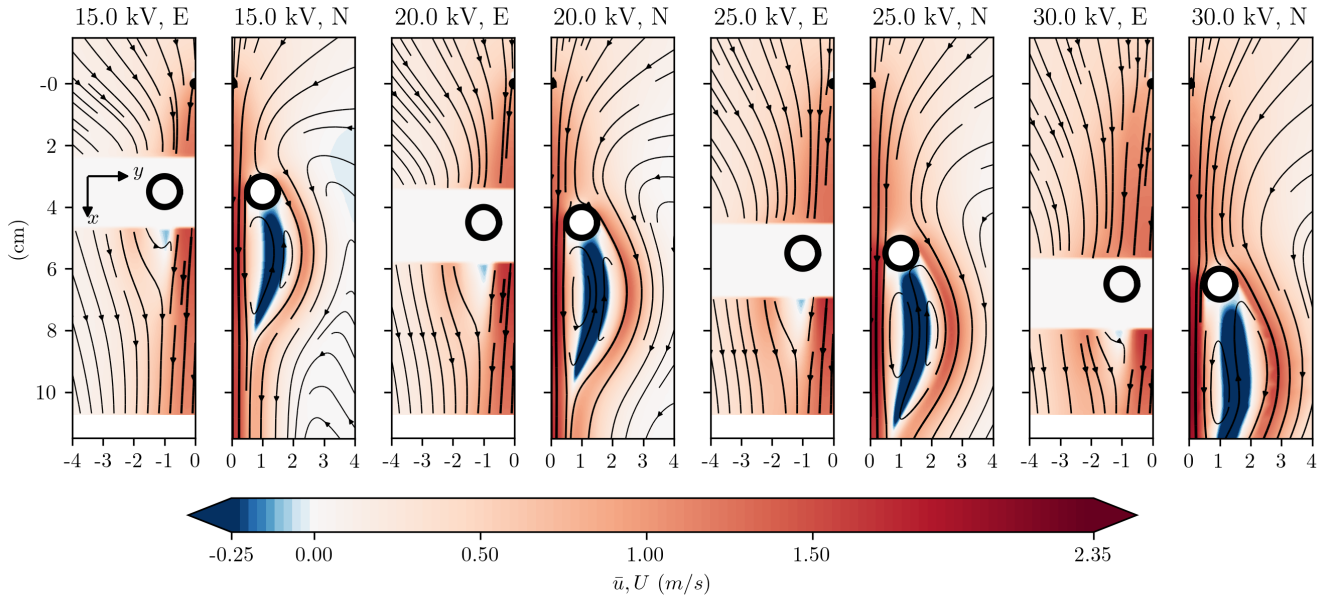

FIG. 6: Same conventions as Fig. 5 when considering the effect of the face-to-face emitter/collector distance $d = 3, 4, 5, 6$cm (from left to right) whilst preserving a constant applied external electric field $E = V/d = 510^5 V/m$ on a 1E/2C configurations ($r_e = 50\mu$ m, $r_c = 1$cm, $s = 2$cm).

comparison between the flow field in the wake region, is poor, as expected.

In the following we will investigate the effect of collector shape changes with constant imposed external electric field precisely because changing the shape will not change at the same time the forcing intensity, permitting an objective comparison between various shapes on propulsive distinguishing features.

B. Exploration of streamlined and multi-electrode configurations

1. *Configurations with single streamlined collector (1E/1S)*

In this section the effect of streamlining the collectors is analyzed, from both physical and aerodynamical viewpoints. The first motivation for analyzing a streamlined collector is obviously coming from aerodynamical consideration associated with wake suppression/drag-reduction. Here, we chose a geometrical shape as close as possible to the cylindrical one, on the upstream face, in order to be able to compare the specific effect of the downstream shape with the least possible perturbation on the upstream electrical field.

In order to exemplify and decipher the main modifications associated with streamlining, figure 7 considers the simplest configuration with one streamlined collector (1E/1S, left panels) and compares the flow field with that obtained for a cylindrical collector (1E/1C, right panels). As expected, the flow is mainly modified in the downstream region : with the streamlined collectors the downstream wake structure is suppressed.

Figure 8(a) describes the variation of the thrust force for 1E/1S configurations versus the aspect ratio, and compares it with the 1E/1C case. The figure shows that streamlining the collector leads to a substantial increase of the total thrust. A priori, one would expect this to be due to a reduction of the aerodynamic drag. Figure 8 shows that it is not the case : the drag T^H_{1E1S} is actually almost insensitive to the aspect ratio. On the other hand, the EAD component of the thrust is enhanced by streamlining, and the increase of the total force is mostly due to this contribution. Note that for the longest collectors ($1 - AR > 0.3$) the aerodynamic drag is actually slightly increased compared to the 1E/1C case, up to about 10% for $1 - AR = 0.08$. This fact seems in opposition with the usual conception of streamlining. However, in the range of Reynolds numbers considered here (of order 10^3 based on the thickness and maximum velocity) the viscous contribution to the drag is not small compared to the pressure contribution, and it increases with the length of the collector.

In order to analyze this substantial effect, Figure 8 also displays the current intensity (b) and the thrust-to-power

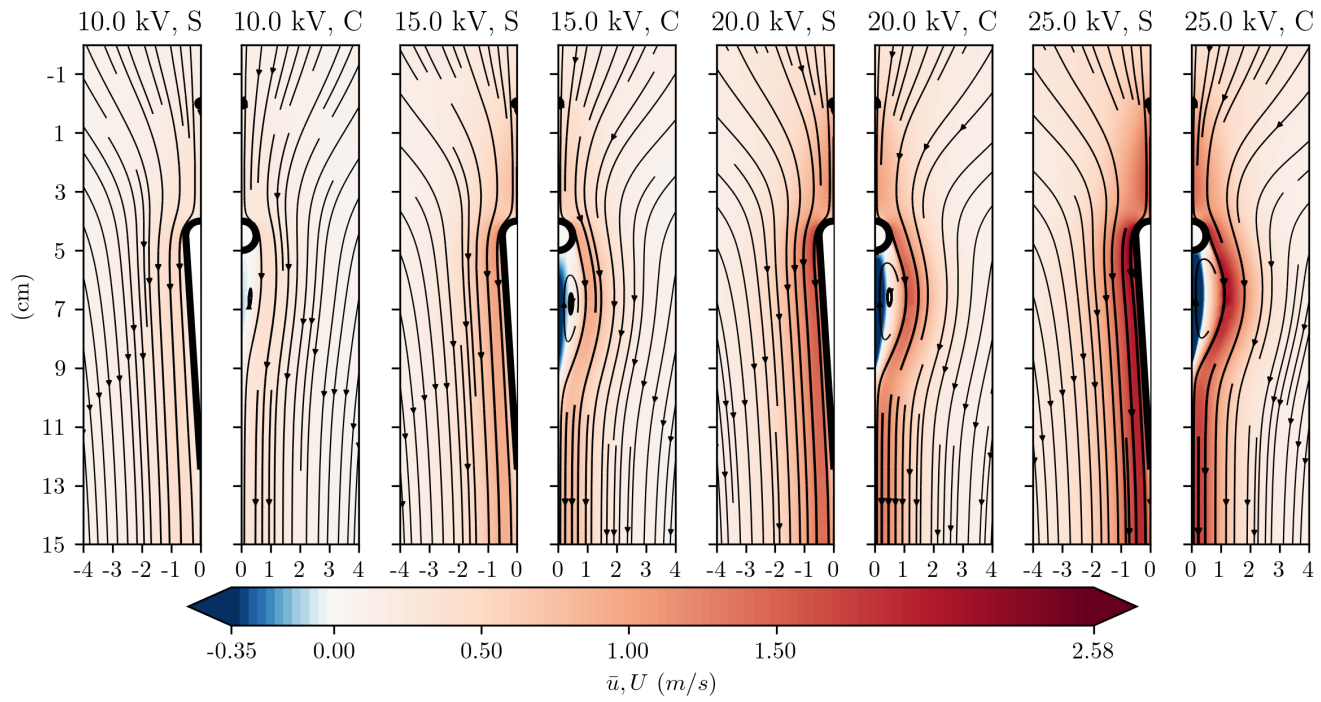

FIG. 7: Representation of ionic wind flow (velocity and streamlines) from simulations, considering a streamlined collector configuration (1E/1S) with aspect ratio $AR = 0.08$ (left panels), compared to a cylindrical collector configuration (1E/1C). The emitter/collector distance is $d = 4$cm and the applied voltage is 10, 15, 20 & 25 kV.

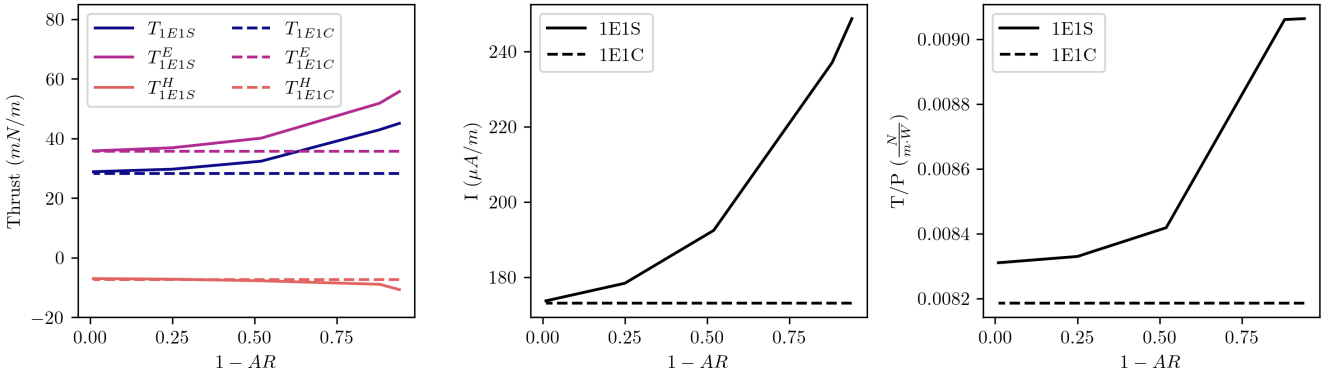

(a) (b) (c)

FIG. 8: Comparison of the propulsive capabilities of single emitter/collector configurations: 1E/1C for a cylindrical collector (dotted lines) vs. 1E/1S for a streamlined one as function of the streamlined aspect ratio AR for an applied voltage $V = 20kV$ and distance $d = 4cm$. (a) : Thrust per unit length; (b) : Current intensity; (c) Thrust-to-power ratio.

ratio (c), both showing a significant improvement when changing the streamlined collector aspect-ratio. These results show that a streamlined collector for ionic wind propulsion is not only interesting for aerodynamic viewpoint but much more from electrical ones. This could seem surprising, at first step, since the chosen configuration was precisely designed to produce a very similar upstream electric field. For this reason the electric field is investigated in the very same configuration in Figure 9. As expected, the electric field lines are very similar for the 1E/1C configuration (left) compared to the 1E/S (right), providing a very similar "direct" charge flux. Nevertheless, even though the intensity of the electric field is lower, one can observe a drastic change in the downstream electric field lines where a much

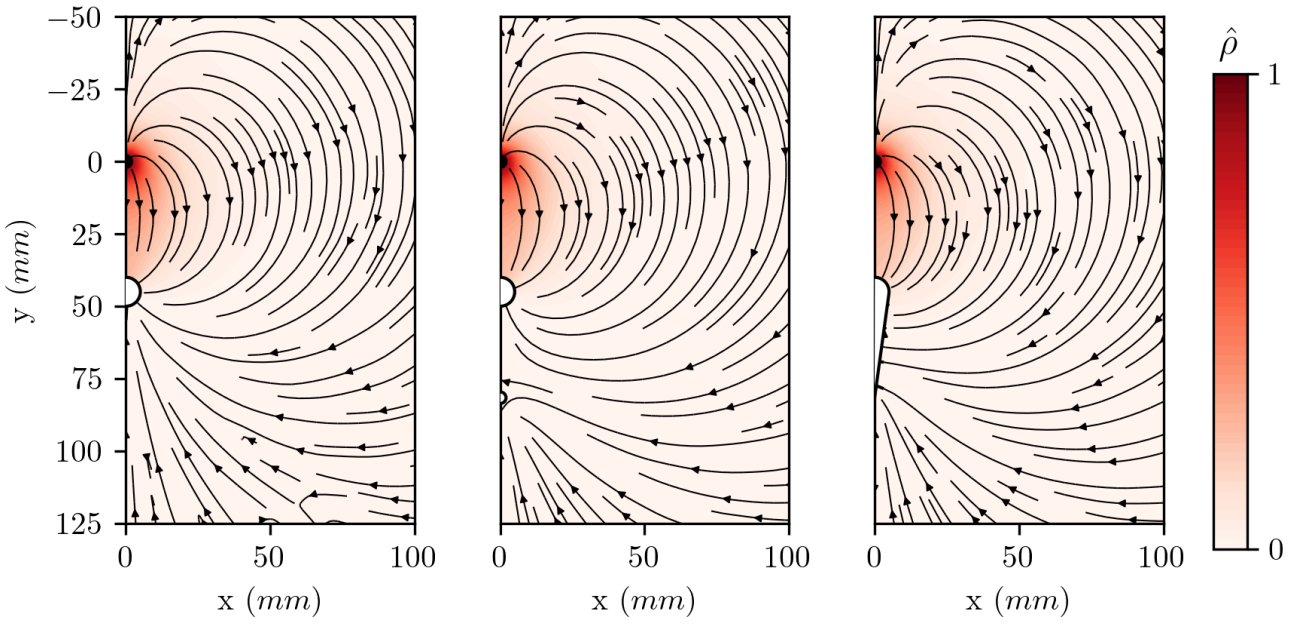

FIG. 9: Visualization of the electric field lines and charge density (colors) for the same configurations as figure 8 ($r_e = 50\mu m, r_c = 1cm$) for three different collector shapes. Left : cylindrical collector, Middle : emitter/collector/collector with $AR = 0.48$, Right Streamlined collector with the same $AR = 0.48$.

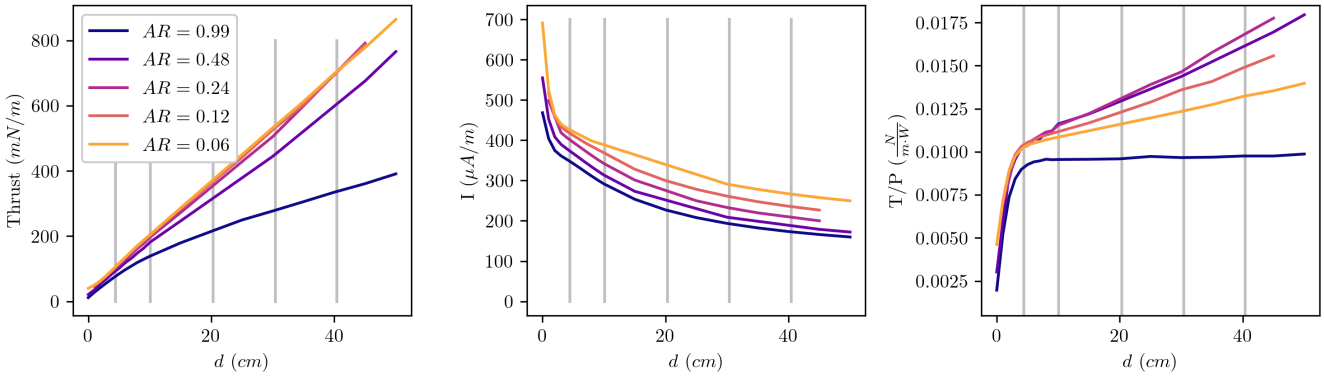

FIG. 10: Propulsive capabilities of centered 1E/2S configurations for an applied external electric field $E = V/d = 5.10^5 V/m$, for various streamlined collectors, having a spacing $s = 4cm$ and different ratio AR. Vertical grey lines represents, from left to right, imposed potential of 25, 50, 100, 150 and 200 kV.

larger region for charge collection is indeed available to the streamlined collector. When examining at the same time the charge density distribution around the collector one can observe that the downstream regions of both 1E/1C & 1E/S configurations display weak charge concentration, whilst at the same time important charge concentration are released upstream the emitter (placed at the origin in Figure 9) resulting from the quasi-isotropic charge concentration at both emitter's surface. Since the charge electro-drift is very dominant over charge diffusion, it is expected that these upstream charge fluxes are finally collected downstream, leading to a secondary 'indirect' current contribution. It turns out that the resulting secondary indirect current for streamlined collector is found to be 11% of the direct one for a $AR = 1/2$ but can build-up to 35% for $AR = 1/5$ as observed in figure 8(b). Although of a surprise is the (slight) improvement on the Thrust-to-Power reported in figure 8(c), indicating that the gain in thrust is not exactly balanced by the indirect current in this configuration.

In order to better analyze the effect of the charge collection improvement in streamlined collectors, a double

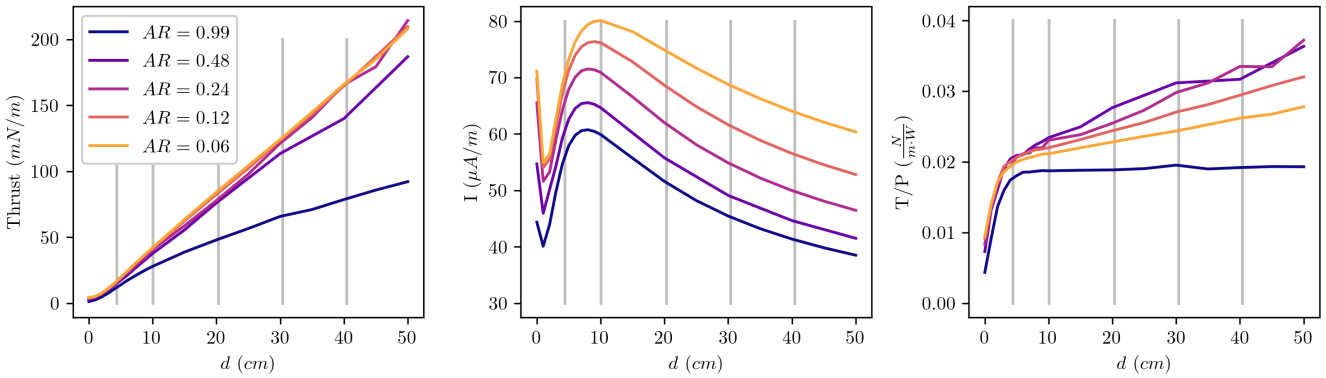

FIG. 11: Propulsive capabilities of centered 1E/2S configurations fo an applied external electric field $E = V/d = 2.5\,10^5 V/m$. Vertical grey lines represents, from left to right, imposed potential of 12.5, 25, 50, 75 and 100 kV.

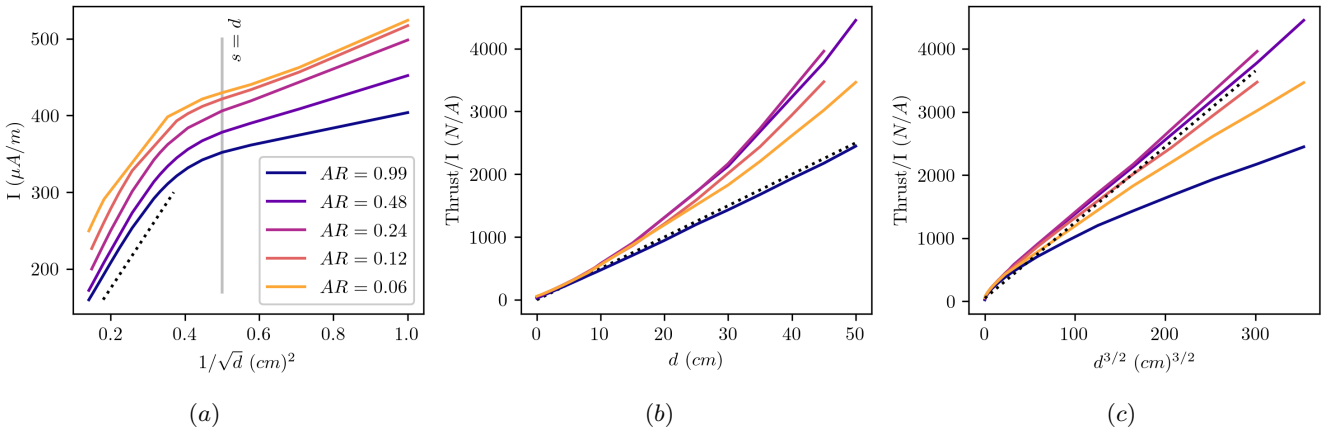

FIG. 12: Same datasets as Figure 10 here investigating relation (1) in the case of streamlined drop-shapes collectors. (a) illustrates the various regime of the lineic density of current intensity I (current per unit length of emitter) versus distance d, also indicating a far-field $I \sim d^{-1/2}$ behavior (dotted line). The vertical grey line shows the value for which d reaches the gap s between collectors, also providing a transition to a distinct I dependency with d at close distances. (b) Dotted line indicates relation (1) ($\mu_p = 2.10^{-4} SI$ value has been chosen). Dark-blue continuous lines is the result for a cylindrical collector which closely coincides with (1). Colored continuous lines gives the behavior of stream-lined shapes. (c) Thrust/I versus $d^{3/2}$ indicating a far-field Thrust $\sim I d^{3/2}$ behavior (provided with dotted lines) for stream-lined drop-shapes.

stage collector (hereby denoted 1E/1C/1C) having the same aspect ratio as the streamlined configuration, is also investigated, so as to analyze the charge collection effect. The middle panel of Figure 9 then shows the electric field lines in this double stage collector, so as to show that, in this case, the electric field lines downstream reconnection might be similar to the streamlined case. However, inspecting the propulsive properties (dotted lines) of this double stage collector configuration in Figure 8 shows no improvement at all in this case. Hence, not only the streamlined collector influences the electrical potential so as to produce electric field lines favorable to charge collection, but at the same time, it influences the charge injection and electro-drift so as to suck more charges out of the emitter. This is why, streamlined collectors are the focus of the next section.

2. Configuration with two streamlined collectors (1E/2S)

Since centered 1E/2C configurations have been found many times [3, 4, 15, 19, 22] to provide the best thrust in open domains, we hereby investigate the influence of streamlined collectors in this configuration. Figure 10 displays the various propulsive quantities when varying the face-to-face distance d between the emitter and the streamlined collector couple when imposing a constant applied external electric field $E = V/d = 5kV/cm$ (or $E = 5\,10^5 V/m$ in SI), i.e V linearly varying as $E.d$. In the case of an quasi-circular shape ($AR = 0.99$), it is found that increasing the distance improves the thrust (Figure 10a) but, at the same time decreases current intensity (Figure 10b) which produces a constant thrust-to-power ratio from perfectly compensated effects (Figure 10c). Increasing the streamlined aspect ratio of the collectors result in an improved thrust (Figure 10a) which display a linear variation with d, the slope of which improves when increasing the aspect ratio up to a saturated trend. This result in an optimal aspect ratio $AR \simeq 1/5$ for which the best thrust can be found together with the best thrust-to-power performance (Figure 10c). A similar pattern is found for a twice smaller imposed electric field $E = 2.5\,10^5 V/m$ as illustrated in Figure 11 with a still optimal streamlined shape having aspect ratio $AR \simeq 1/5$.

When deepening the analysis of Figures 10 and 11, it is first interesting to notice that the current behavior in Figure 10b and Figure 11b display two distinct regimes depending on the relative values between the distance d to collector spacing s. At very short distance, i.e. for $d \ll s$ a non-monotonous behavior is found whereas at larger distances, i.e. for $d \gg s$ the current decays for any considered shape of collector, following a somehow generic decay law, for both streamlined and cylindrical collectors.

To analyse this generic decay law and compare it with previous experiments and available models, let us first recall that the most established model of intensity as function of applied voltage is Townsend's law,

$$I = C(d)V(V - V_0), \tag{13}$$

in which dependence upon the distance d is incorporated into the Townsend pre-factor $C(d)$. When increasing the distance and keeping the "external electric field" V/d constant, considering voltages much larger than the critical voltage V_0, this law implies $I \sim d^2 C(d)$. Figure 12(a) reconsiders the data of Figure 10(b), and suggests that the intensity scales as $I \sim d^{-1/2}$ for $d \gg s$ and constant "external electric field" V/d. The cross-over to this far-field regime is found when $d \sim s$ (vertical line of figure 10a) as also suggested in [24] where the distance gap to collector spacing ratio was identified as an important parameter. This result suggests that the role of spacing s is "screened" for large distance d when the electro-static effect of the two collectors can mostly be identified as a single one, resulting in a generic far-field electric potential and electric field decay. On the contrary, when d is smaller or comparable to s, one expects a specific, configuration and shape dependant behavior of the current variation with d. In this case, the principal current fluxes from emitter to collectors are following the shortest path, the length of which strongly depends on s. The $I \sim d^{-1/2}$ far-field scaling imply a $C(d) \sim d^{-5/2}$ one for the Townsend pre-factor. This differs from the experimental observation that $C(d) \sim d^{-2}$ which was proposed as a fit of experimental results obtained with cylindrical collectors, at constant applied potential, when varying distance d by [18, 28]. In order to understand this discrepancy, we revisit the scaling dependence of the Townsend law pre-factor using the experimental data of [18, 28] (Cf Appendix V). We show in Appendix V that $C(d) \sim d^{-5/2}$ either provides an equal or perhaps better fit of the experimental data. Hence, given the available data points, a $C(d) \sim d^{-5/2}$ decay of the Townsend law pre-factor is consistent with experimental observations, and thus also consistent with our reported numerical results.

Considering now the thrust of a cylindrical collector, figure 12b recovers (1). The total trust force associated with the cylindrical collector found in figure 12b again indicates a small contribution of the air drag in the absence of an imposed external flow, since relation (1) is find very close to numerical results although it does not take into account the drag contribution. For bluff-body shaped configuration (1) has been theoretically derived for arbitrary configurations of collectors from physical [19] or asymptotic [21] arguments. Relation (1) however fails to describe the case of streamlined drop-shaped collectors as also shown in figure 12b. Numerical results provided in figure 12c better suggest that, in the case of streamlined drop-shapes, when imposing a constant external electric field $E^{ext} = V/d$, the far-field $d \gg r_c$ thrust to intensity relation reads

$$\mathrm{T} \sim \frac{Is}{\mu}\left(\frac{d}{s}\right)^{3/2}. \tag{14}$$

Relation (14) is also consistent with the linear behavior of the thrust for increasing distance at fixed external field $E^{ext} = V/d$ found in figure 11a for streamlined shapes, from the previously discussed $I \sim d^{-1/2}$ behavior found in figure 10b.

Hence, from a quantitative view-point, the far-field behavior of streamlined collectors configurations differs from the cylindrical shapes ones, the analysis of which can bring significant impact on the propulsive capabilities. This brings the issue of whether these improved propulsion features could be exploited in parallel emitter/streamlined collectors configurations.

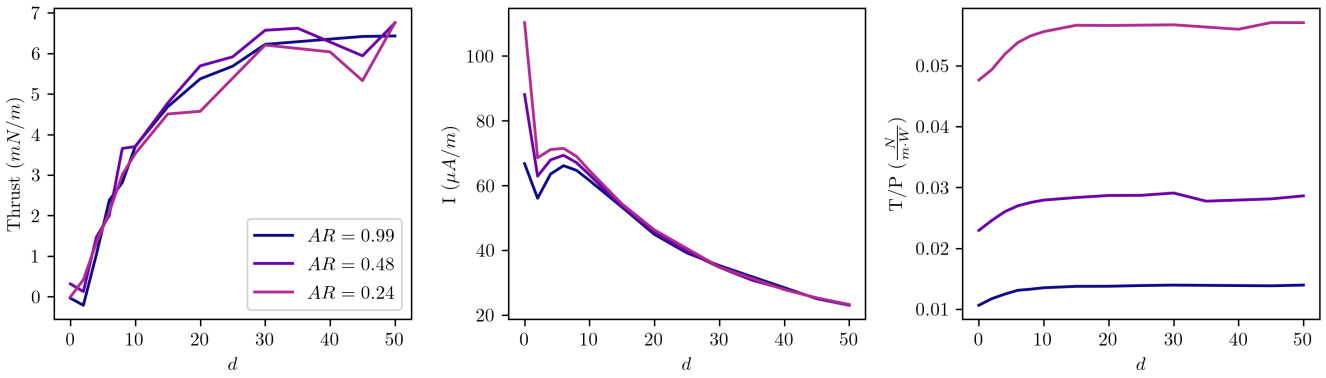

(a) (b) (c)

FIG. 13: Propulsive capabilities of a periodic (NE/NS) configurations of staggered cylindrical emitter/collectors versus the distance d between electrodes. A constant electric field $E = V/D = 2.5kV/cm$ is imposed, and the collectors span-wise spacing is $s = 60mm$.

3. *Periodic emitter/streamlined collector configurations (NE/NS)*

.

We now investigate the propulsive features of a periodic array of streamlined collectors depicted in Figure 1d where the relevant geometrical parameters are illustrated.

Figure 13(a) provides the propulsion thrust associated with a periodic array of emitter/collector electrodes separated by a span-wise distance $s = 60mm$, for various emitter/collector distances d. For d smaller than s, an increase of thrust when increasing distance d is recovered, similarly with the trend found in figure 10(a). Nevertheless, as distance d is increased the thrust levels-down, reaching a quasi-constant value, as d gets close to periodicity s. This result in a total thrust per unit-length smaller by almost two-orders of magnitude from the non-periodic configuration at a distance comparable to figure 10(a). A similar observation can be deduced for the current intensity from comparing figure 13(b) to figure 10(b). The two regimes of the intensity variation with distances are qualitatively recovered, but the magnitude of the intensity is much lower in the periodic case. Interestingly enough, the thrust-to-power ratio of streamlined configurations saturates with increasing distances in the case of periodic configurations (figure 13(c)) as opposed to the open configurations shown in figure 10(c). This saturation of the thrust-to-power ratio is similar to the one obtained for cylindrical collector in open configurations also displayed in figure 10(c). This remark pin-points the physics behind this observation. For cylindrical collectors, we found less extended electric field lines around the collector shape being the reason for lower current collection at the collector. The electric field lines associated with streamlined collectors in open configuration were indeed found much transversely extended, permitting more charge recovery and thus more current intensity to be collected. Now realizing that span-wise distance s of transversely periodic configuration is a limiting distance for the transverse extension of electric field lines permit to understand that a periodic array of streamlined collector behaves very differently from a single one. In the periodic case, the streamlined collector electric fields lines are electrostatically screening each other, as emitters does, as studied in [14]. Hence the detrimental effect of transverse periodicity of the emitter/collector system is closely related to the electric field confinement.

4. *Effect of inlet velocity*

Let us consider, finally, the propulsive performances of a periodic array of electrodes (NE/NS) in the case where the electrodes are moving at a constant velocity with respect to the fluid. This case is investigated by solving the equations of Sec. II B considering an imposed "inlet velocity", U_{in}, now considered as a physical parameter, instead of a numerical regularization parameter required to be small, as explained in appendix IV. As previously discussed in section II B, we consider inlet velocity U_{in} of few meter per second so that, since the electro-convective velocity ratio is small i.e $M_{ce} = U/\mu E^{ext} \ll 1$, the advection effects are neglected. Hence in this one-way coupling framework there is no back-coupling of the flow into the ion transport problem, and no need to take into account the background flow for the electric problem. Taking into account two-way coupling effects is an interesting issue which is beyond the scope of the present study.

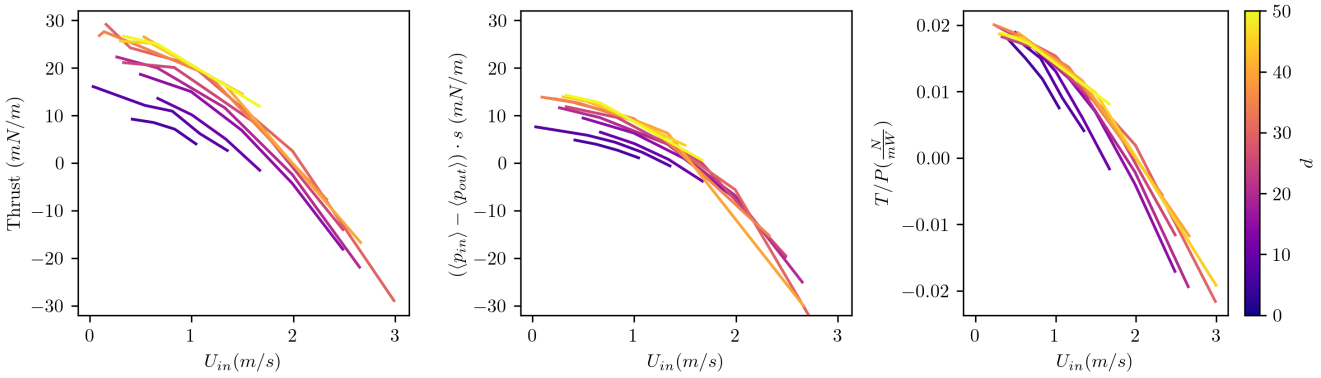

FIG. 14: Propulsive capabilities of a periodic (NE/NS) configurations of staggered cylindrical emitter/collectors versus the Inlet velocity U_{in}. A constant electric field $E = V/D = 2.5kV/cm$ is imposed, and the collectors span-wise spacing is $s = 60mm$.

The influence of the inlet velocity is analyzed in figure 14. As expected, increasing the inlet velocity decreases the thrust, because the drag negatively contributes to the thrust and becomes more and more predominant for increasing U_{in}. The associated Reynolds number $\rho_f U_{in} 2r_c/\mu_f$ based upon the collector front diameter $2r_c$ is varied from 10^{-2} to 5.10^3. The observed effect can be attributed to the inertial pressure being a quadratic function of U_{in}, from the parabolic shape of the thrust observed in figure 14(a). Furthermore, when comparing the total thrust with the overall inlet-outlet pressure drop, a very similar trend is found in figure 14(b), testifying that the pressure contribution to the drag is predominant. The thrust-to-power ratio also drops-down quite significantly with increasing inlet velocity as shown in figure 14(c). As can be observed using the color-coded legend of figure 14, the performances, i.e the thrust in figure 14(a) and the thrust-to-power in figure 14(c), are slightly improved for large gap d. Nevertheless, since in this one-way coupling regime, the EAD thrust T^E does not depend on the applied velocity whereas the drag is increasing quadratically with it, i.e $T^H \sim \rho_f U_{in}^2 A$ —where $A = r_c.L$ is the front area based upon the collector front diameter $2r_c$ and its length L—, T^E is rapidly dominated by T^H. Neutral effects, i.e the exact balance between T^E and T^H per-unit-length —both T^E & T^H scale linearly with L— arise in the case of $r_c = 1cm$ and collector gap distance $s = 60cm$ for inlet velocities U_{in} in the range $1 - 2m/s$. This figure is interesting to mention for further experimental measurements and/or calibration. Last, but not least, it is important to mention that even if aerodynamic effects have been taken into account rather precisely in the reported computations, only stationary predictions associated with steady base flows are provided. Nevertheless, wake instabilities are known to develop for moderate Reynolds number behind bluff bodies (e.g a critical Reynolds number values as small as 48 is found for a cylinder shape [29]). For elongated bodies such as the hereby studied streamlined drop shapes the critical Reynolds number is found within the range of $10^3 - 10^5$, which strongly depends on the maximum thickness of airfoil profile [30]. Hence possible un-stationary effects might affect the drag at higher Reynolds number which have been discarded here. This has to be born in mind for more refined investigations as well as future experimental comparisons.

IV. CONCLUSION

This paper numerically analyses the ionic wind generation in various emitter/collector configurations using a drift-diffusion model for the electrostatic problem, and a one-way coupling one for the aerodynamic problem. Using 2D domains of sufficient dimension to minimize confinement effects (enabled by the intensive use of adapted mesh) we analyze a wide range of geometrical and electrical configurations. We found that aerodynamic drag can significantly affect the net thrust, thus enhancing the prediction quality of atmospheric EAD propulsive systems performances. Then, accounting for aerodynamic thrust allows for a quantitative match with previous experimental observations within 1%. Comforted by the relevance of this direct approach of ionic wind modeling, we analyze various configurations having either one emitter and two collectors or a transversely periodic array of electrodes. The effect of streamlined collectors having drop-shape has also been carefully analyzed, from a systematic analysis of the influence of its aspect ratio. In the case of open-configuration having one emitter and two collectors, we found a significant improvement in every propulsive capacities for streamlined collectors. An optimal aspect ratio of 0.25 has been found for which the thrust to power and the thrust are the best. Also a linear increase of thrust with emitter/collector

distance when imposing a constant "external" electric field V/d has been found. Obviously reaching very high tension in order to benefit from these improved propulsion performances at large distance d has to be tempered from the known appearance of "streamer regime" being more sensitive at very high tensions, in experiments.

In the case of transversely periodic arrays of emitter/collectors, the effect of streamlined collectors on propulsive performances has been found poor. The performance degradation has been identified to the electric-field line confinement. This result is also consistent with previous experimental observation of performance degradation for periodically transverse configurations. Finally, the far-field behavior of the thrust and current intensity have been analyzed and found distinct for cylindrical or streamlined collector shape. A deeper understanding of these far-field behaviors might be of interest in future studies, but this issue is beyond the scope of the present contribution.

APPENDIX :REMARKS ON THE BOUNDARY CONDITIONS FOR FLUID FLOW EQUATIONS

The numerical modeling of 2D incompressible jets poses a difficulty in the choice of boundary conditions. This effect is related to the fact that since the jet has a nonzero flow rate across the outlet boundary, a "flow entrainement" of the surrounding air, coming from the outer parts of the domain, has to occur tu supply a flow rate balancing the one carried out by the jet. This entrainement is expected to lead to "confinement effets" affecting the results, especially in 2D where the entrainement flow decays much more slowly with distance compared to 3D (namely, considering a potential sink as a first approximation of entrainement, a decay as $|\mathbf{u}| \approx r^{-1}$ for 2D compared to $|\mathbf{u}| \approx r^{-2}$ for 3D), and in situations where the fluid away from the electrodes is expected to be quiescent.

The most obvious choice of boundary conditions for the present problem would be to impose a zero velocity at both the inlet and lateral boundaries, and a no-stress condition at the outlet boundary. However, with this choice, the only possibility is for entrained flow to originate from the remote portions of the outlet boundary, located far away from the jet. Thus, there would be flow coming "in" through a boundary treated as an "outlet", leading to divergence in the Newton iteration.

To avoid this and to allow an entrainment flow coming from the upper regions of the mesh, we designed a simple method which consists of using an imposed "inlet velocity" U_{in} at the inlet boundary, the integral of which over $\partial\Omega_{in}$ balancing the flow rate carried out by the jet through $\partial\Omega_{out}$. A free-stress condition is then imposed on both the outlet boundary $\partial\Omega_{out}$ and the lateral boundaries $\partial\Omega_{top}, \partial\Omega_{bot}$. This choice allows the balance between the imposed flow entering through $\partial\Omega_{in}$ and the one leaving the domain through $\partial\Omega_{out}$ to be implicitly taken care-off. Using this fairly straightforward approach, increasing the domain size permits to diminish the value of U_{in} when trying to model a zero far-field at infinity. We found numerically a quasi-linear relation between U_{in} and thrust as illustrated in figure 15 in the of a 1E/1C configuration case. This figure also illustrates the decreasing influence of U_{in} as the domain size is increased, up to 500 collector diameter in the presented example. Thus, a pragmatic convergence criteria can be set up by decreasing U_{in} value and increasing domains, so as to obtain change in the propulsion force less than 0.5%.

V. TOWNSEND-LAW PREFACTOR $C(d)$ FAR-FIELD BEHAVIOR

In this section we revisit the far-field current of cylindrical emitter/collector systems. Two experimental studies [18, 28] have measured the current-intensity relation in 1E1C configuration and reported the Townsend prefactor $C(d)$ of the current-intensity relation (1) variation with distance d. Both report a $C(d) \sim d^{-2}$ decay as previously suggested by other authors, reported in figure 16. Nevertheless, our numerical simulations suggest a slightly different scaling $C(d) \sim d^{-5/2}$ also reported in figure 16. In each cases figure 16 displays the linear fits. Given the available data points in the reported range of d it seems that both scaling are compatible with available observations without clearly distinguishable best-one.

FUNDING SOURCES

This research has been funded by the ANR Astrid, ANR-20-ASTC-0029-02.

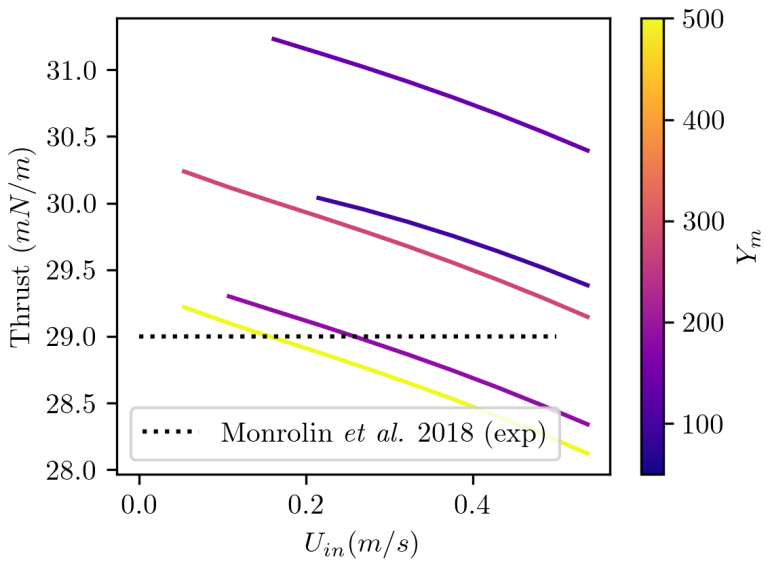

FIG. 15: Thrust measured on a 1E1C configuration, having $d = 40mm$ and applied voltage of $20kV$, as a function of domain size and blowing intensity. Dashed line represents the thrust measured experimentally

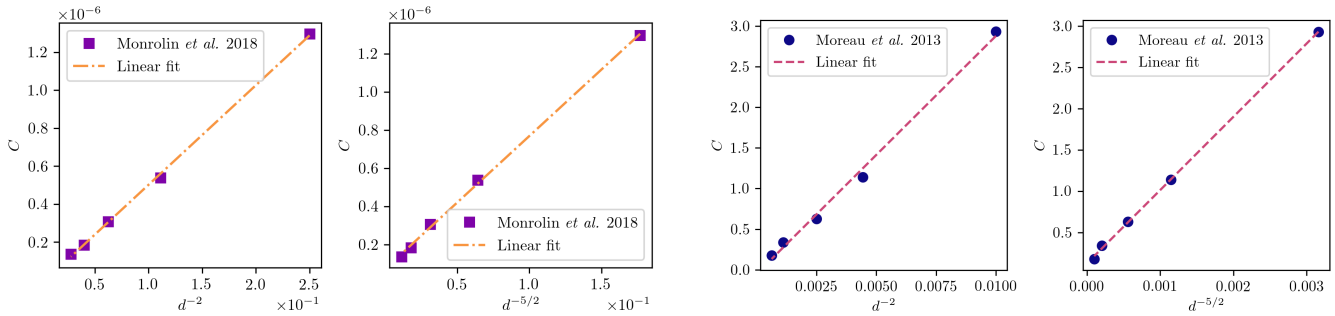

(a) (b)

FIG. 16: Comparison between two posssible scalings for Townsend law (1)'s prefactor $C(d)$ versus the emitter-collector distance d for a 1E1C configuration. (a) data from [28]. (b) data from [18].

ACKNOWLEDGMENTS

We thanks E. Moreau, S. Grosse and N. Binder for fruitful exchanges and discussion. This work is under a CC-BY 4.0 licence.

[1] Xu, H., He, Y., Strobel, K. L., Gilmore, C. K., Kelley, S. P., Hennick, C. C., Sebastian, T., Woolston, M. R., Perreault, D. J., and Barrett, S. R. H., "Flight of an aeroplane with solid-state propulsion," Nature, Vol. 563, No. 7732, 2018, pp. 532+.

[2] Xu, H., Gomez-Vega, N., Agrawal, D. R., and Barrett, S. R., "Higher thrust-to-power with large electrode gap spacing electroaerodynamic devices for aircraft propulsion," J. Phys. D. Appl. Phys., Vol. 53, No. 2, 2020.

[3] Khomich, V. Y., and Rebrov, I. E., "In-atmosphere electrohydrodynamic propulsion aircraft with wireless supply onboard," J. Electrostat., Vol. 95, 2018, pp. 1–12.

[4] Belan, M., Arosti, L., Polatti, R., Maggi, F., Fiorini, S., and Sottovia, F., "A parametric study of electrodes geometries for atmospheric electrohydrodynamic propulsion," J. Electrostat., Vol. 113, 2021.

[5] Rebrov, I. E., and Khomich, V. Y., "Formation of Electrohydrodynamic Flow in Corona Discharge of a Three-Cascade Electrode System with Serial and Alternating Connection," Plasma Phys. Rep., Vol. 47, No. 1, 2021, pp. 105–109.

[6] Gomez-Vega, N., Xu, H., Abel, J. M., and Barrett, S. R. H., "Performance of decoupled electroaerodynamic thrusters," Appl. Phys. Lett., Vol. 118, No. 7, 2021.

[7] Xu, H., Gomez-Vega, N., Wilde, N. D., Kambhampaty, J. D., and Barrett, S. R. H., "Electrical characteristics of wire-to-wire dielectric barrier discharges," Plasma Sources Sci. T., Vol. 30, No. 8, 2021.

[8] Monrolin, N., and Plouraboué, F., "Multi-scale two-domain numerical modeling of stationary positive DC corona discharge/drift-region coupling ," J. Comput. Phys., Vol. 443, 2021, p. 110517.

[9] Adamiak, K., and Atten, P., "Simulation of corona discharge in point plane configuration," J. Electrostat., Vol. 61, No. 2, 2004, pp. 85–98. URL `http://linkinghub.elsevier.com/retrieve/pii/S030438860400035X`.

[10] Zhao, L., and Adamiak, K., "Numerical simulation of the electrohydrodynamic flow in a single wire plate electrostatic precipitator," IEEE T. Ind. Appl., Vol. 44, No. 3, 2008, pp. 683–691.

[11] Peek, F. W., Dielectric phenomena in high voltage engineering, McGrow-Hill Book Company, New-York, 1915.

[12] Monrolin, N., Praud, O., and Plouraboué, F., "Revisiting the positive DC corona discharge theory: Beyond Peek's and Townsend's law," Phys. Plasmas, Vol. 25, 2018, p. 063503.

[13] Johnson, M. J., and Go, D. B., "Recent advances in electrohydrodynamic pumps operated by ionic winds: A review," Plasma Sources Sci. T., Vol. 26, No. 10, 2017.

[14] Lemetayer, J., Marion, C., Fabre, D., and Plouraboué, F., "Multi-inception patterns of emitter array/collector systems in DC corona discharge," Journal of Physics D: Applied Physics, Vol. 55, No. 18, 2022, p. 185203.

[15] Belan, M., Terenzi, R., Trovato, S., and Usuelli, D., "Effects of the emitters density on the performance of an atmospheric ionic thruster," J. Electrostat., Vol. 120, 2022.

[16] Gomez-Vega, N., Brown, A., Xu, H., , and Barrett, S. R. H., "A model of multi-staged ducted thrusters for high-thrustdensity electroaerodynamic propulsion," AIAA. J., 2022.

[17] Christenson, E., and Moller, P., "Ion-Neutral Propulsion in Atmospheric Media," AIAA. J., Vol. 5, No. 10, 1967, pp. 1768–1773. doi:10.2514/3.4302.

[18] Moreau, E., Nicolas, B., Jean-Daniel, L.-S.-L., and Jean-Pierre, C., "Electrohydrodynamic force produced by a wire-to-cylinder dc corona discharge in air at atmospheric pressure," J. Phys. D: Appl. Phys., Vol. 46, No. 47, 2013, p. 475204.

[19] Gilmore, C. K., and Barrett, S. R. H., "Electrohydrodynamic thrust density using positive corona-induced ionic winds for in-atmosphere propulsion," Proc. R. Soc. A, Vol. 471, No. 2175, 2015, pp. 20140912–20140912.

[20] Vaddi, R. S., Guan, Y., Mamishev, A., and Novosselov, I., "Analytical model for electrohydrodynamic thrust," Proc. R. Soc. A, Vol. 476, No. 2241, 2020.

[21] Monrolin, N., Praud, O., and Plouraboué, F., "Electrohydrodynamic ionic wind, force field, and ionic mobility in a positive dc wire-to-cylinders corona discharge in air," Phys. Rev. Fluids, Vol. 3, No. 6, 2018, p. 063701.

[22] Coseru S., D., Fabre, and Plouraboué, F., "Numerical study of ElectroAeroDynamic force and current resulting from ionic wind in emitter/collector systems," J. Phys. D: Appl. Phys., Vol. 129, No. 10, 2021, pp. 85–96.

[23] Adamiak, K., "Quasi-stationary modeling of the DBD plasma flow control around airfoil Quasi-stationary modeling of the DBD plasma flow control around airfoil," Phys. Fluids, Vol. 085108, 2020.

[24] Kahol, O., Belan, M., Pacchiani, M., and Montenero, D., "Scaling relations for the geometry of wire-to-airfoil atmospheric ionic thrusters," J. Electrostat., Vol. 123, 2023.

[25] Hecht, F., "New development in FreeFem++," J. Numer. Math., Vol. 20, No. 3-4, 2012, pp. 251–265. URL `https://freefem.org/`.

[26] Fabre, D., Citro, V., Ferreira Sabino, D., Bonnefis, P., Sierra, J., Giannetti, F., and Pigou, M., "A Practical Review on Linear and Nonlinear Global Approaches to Flow Instabilities," Applied Mechanics Reviews, Vol. 70, No. 6, 2019. 060802.

[27] Kiousis, K. N., Moronis, A. X., and Fruh, W. G., "Electro-Hydrodynamic (EHD) Thrust Analysis in Wire-Cylinder Electrode Arrangement," Plasma Sci. Technol., Vol. 16, No. 4, 2014, pp. 363–369.

[28] Monrolin, N., Plouraboué, F., and Praud, O., "Electrohydrodynamic Thrust for In-Atmosphere Propulsion," AIAA. J., Vol. 55, No. 12, 2017, pp. 4296–4305.

[29] Williamson, C. H. K., "Oblique and parallel modes of vortex shedding in the wake of a circular-cylinder at low reynolds-numbers," J. Fluid Mech., Vol. 206, 1989, pp. 579–627.

[30] Carmichael, B. H., "Low Reynolds Number Airfoil Survey," NASA Report No. 165803, Vol. 206, 1981, pp. 579–627.